

Structural, Morphological and Antibacterial Studies of Solvothermally Synthesized ZnS Nanostructures: Effects of Sulphur Precursors

Lalita Rani* & R P Chauhan

Department of Physics, National Institute of Technology, Kurukshetra 136 119, India

Received: 10 May 2023; Accepted: 30 May 2023

The study of zinc sulphide semiconducting nanostructures for antibacterial applications is widely increasing. As the treatment of many infectious diseases is still challenging and efforts are being made to control the growth of bacterial infection. The present work focuses on the structural, morphological, elemental, optical and antibacterial studies of zinc sulphide (ZnS) semiconducting nanostructures synthesized using different sulphur sources. Solvothermal method is used as it is one of the most promising methods to synthesize nanostructures by controlling the reaction time and reaction temperature under high pressure. The X-ray diffraction (XRD) results give the zinc blende crystal structure for both ZnS nanostructures with crystallite size lies in the range 3 to 4nm. The prominent change in the morphology of the synthesized nanostructures is shown by scanning electron microscopy (SEM). Energy dispersive X-ray spectroscopy (EDX) provides information regarding the elemental framework and type of chemical bonding present is as done by Fourier transform infrared spectroscopy (FTIR). The luminescence and bandgap determination are done by photoluminescence (PL) spectroscopy and UV-visible absorption spectroscopy. The synthesized nanostructures are efficient in the degradation of the cell membrane of *Escherichia coli* (*E. coli*) and *Staphylococcus aureus* (*S. aureus*) bacterial families. The production of reactive oxygen species (ROS) is the dominating mechanism of action responsible for the degradation of cell membrane causing cell death. They may be further used for other applications such as an antioxidant and photo catalytic degradation etc.

Keywords: Zinc Sulphide (ZnS), Nanostructures (NSs), Zinc Acetate Zn (Ac)₂ and Reactive Oxygen Species (ROS)

1 Introduction

The study of II-VI semiconducting nanostructures is extensively increasing due to their multifaceted applications in different fields such as catalysis, optoelectronics, antibacterial studies, solar cells etc¹⁻⁵. Zinc sulphide is chosen out of other II-VI family members due to its deeper bandgap of around 3.68 eV for bulk which increases as we move to nanoscale. We are interested to study at nanoscale as the properties of the material changes drastically at nano scale, such as the bandgap and surface area increases due to quantum confinement effect. Also ZnS has multifaceted applications in various fields such as LEDs, supercapacitors, water purification, photo catalytic degradation, solar cells etc⁶⁻¹⁰. For example, in biological fields ZnS after tuning its bandgap acts as a reactive agent against photocatalysis disinfection and water decontamination etc.¹¹ ZnS exists in two crystalline forms namely zinc blende (sphalerite) and hexagonal (wurtzite). It exhibits n-type conductivity and is much stable than the other members in the II-VI family semiconductor compounds.

Due to its wide bandgap the generation of electrons and holes can easily takes place in conduction band and valence band which results in the formation of free radicals under UV-light irradiation. The free radicals can further generate reactive oxygen species (ROS) which are responsible for the inhibition of growth of bacterial families¹²⁻¹⁴.

ZnS can be synthesized in zero, one and two dimensions but as we know that the properties are enhanced as lower is the dimension. So we are synthesizing zero dimensional zinc sulphide semiconducting nanostructures. Plenty of techniques are used to synthesize ZnS nanostructures such as co-precipitation, electrodeposition, solvothermal etc. Present work focuses on the solvothermal synthesis of ZnS nanostructures by controlling the reaction temperature and time under high pressure. The morphology of nanostructures is changed by using different sulphur precursors¹⁵. Morphology plays a significant role in restricting the growth of bacterial families. To the best of author knowledge, no work has been done in the literature showing that the thiourea based sample is more effective to kill the bacterial species compared to the sodium sulphide precursor based sample.

*Corresponding author (E- mail: Lalitarani7194@gmail.com)

2 Materials and Methods

2.1 Materials

The synthesis of zinc sulphide semiconducting nanostructures is done by using zinc acetate dehydrate (99.8%, AR), thiourea (98%) and sodium sulphide (98.55%) purchased from Loba Chemie and are of high purity analytical grade chemicals. De-ionized water purchased from Merck is used as a solvent. All these chemicals are used as obtained without any further purification.

2.2 Preparation of ZnS nanoparticles

To prepare sample A, zinc acetate dehydrate is added in 30ml of de-ionized water and stirred for 45 minutes. Meanwhile, on the other side the homogeneous solution II is obtained by adding sodium sulphide in 30ml of de-ionized water and stirred for 45 minutes. Solution II is added to solution I and the final solution is further stirred until a transparent solution is obtained and then finally transferred to an autoclave of 120ml capacity and placed in an oven at 200°C for 3 hours and 45 minutes. The filtrate is washed with acetone and de-ionized water multiple times to remove any soluble impurity and kept on drying at 50°C for 15 hours. To prepare sample B, thiourea is added instead of sodium sulphide and the similar procedure is followed as mentioned above. The obtained dried powdered samples are used for characterizations and the flowchart given in Fig. 1 represents the steps performed during the synthesis of zinc sulphide nanostructures.

2.3 Characterizations

The crystal structure is determined by Rigaku miniflex –II X-ray diffractometer which uses a 1.54 angstrom Cu K_{α} radiation to inspect the sample. The optical absorption studies are done

using SHIMADZU UV-3600 plus UV-VIS-NIR spectrophotometer and emission spectroscopy by Shimadzu RF5301PC spectrophotometer. The EDX and FTIR analysis are done using OXFORD INSTRUMENTS energy dispersive spectrophotometer and BRUKER spectrophotometer. JEOL/EO JSM-6390 SEM gives the topographical and morphological information.

3 Results and Discussions

3.1 Structural analysis

The synthesized powdered samples show zinc blende cubic structure as examined by X-ray diffraction spectroscopy. Figure 2 shows the corresponding peak position with respect to intensity in the 2θ range of 20° to 70°. The miller planes for

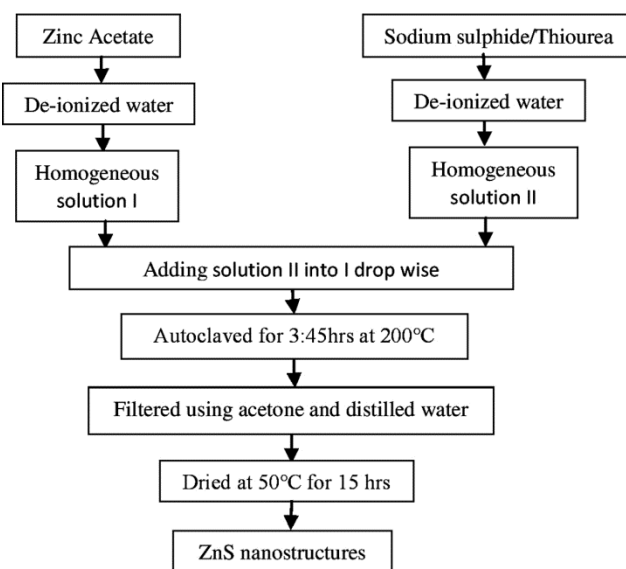


Fig. 1 — Flowchart specified the various steps followed during the synthesis of ZnS nanostructures.

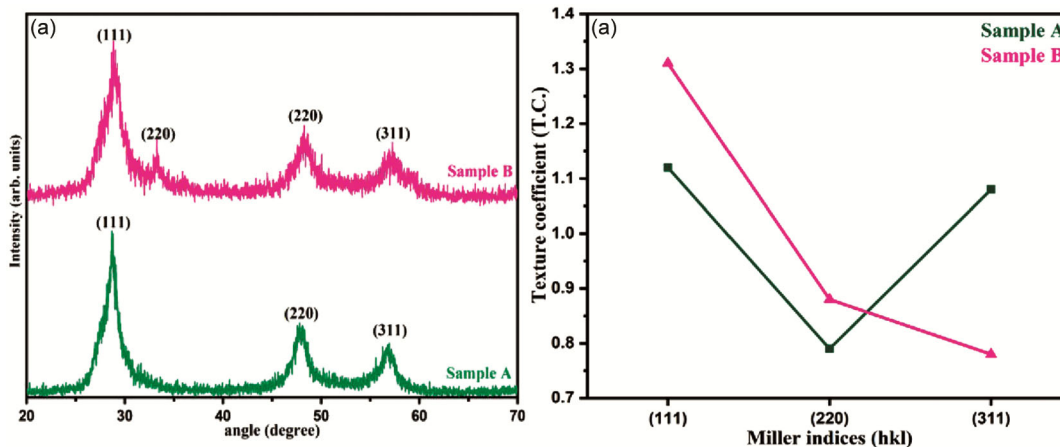


Fig. 2 — (a) Powdered X-ray diffraction analysis, and (b) Texture coefficient with respect to miller indices.

sample A corresponding to peak positions 28.62°, 47.92°, and 56.67° resembles with the JCPDS card number # 65-5476 and for sample B the corresponding peak position 28.83°, 48.29° and 57.16° resembles with the JCPDS card number #80-0020. No change in phase is observed and the average crystallite size lies between 3-4 nm as calculated by Debye and Scherrer's formula¹⁶ as given in equation 1

$$D = k\lambda/\beta\cos\theta \quad \dots (1)$$

Where D denotes the average crystallite size, value of k lies in the range of 0.95 to 0.98, value λ is equal to 1.54Å which is the incident wavelength of Cu-K α light used for detection, β is the full width at half maxima (FWHM), θ is the diffraction angle given by bragg. The interplanar spacing is also calculated by Bragg's diffraction formula¹⁷ given by equation 2

$$d = \frac{n\lambda}{2\sin\theta} \quad \dots (2)$$

Where n represents the order of diffraction, λ is the wavelength of light used and θ is Bragg's diffraction angle. The strain generated during the synthesis due to distortion and imperfection in the crystal as the particle size reaches to nano is calculated by stokes and Wilson¹⁸ equation 3 as given below

$$\varepsilon = \frac{\beta}{4\tan\theta} \quad \dots (3)$$

Where β is the full width at half maxima, ε is the generated strain, and θ is the bragg's angle. The parameter δ denotes the dislocation density determines the perfection of the crystal calculated by the formula¹⁹ given in equation 4

$$\delta = \frac{1}{D^2} \quad \dots (4)$$

Table 1 shows the calculated values of strain, crystallite size, interplanar spacing, dislocation density and full width at half maxima. The variation in the intensity and morphology of the synthesized nanostructures depends on the preferred orientation²⁰ of the miller planes calculated using equation 5

$$TC = \frac{I(hkl)/I_o(hkl)}{1/n\sum(I(hkl)/I_o(hkl))} \quad \dots (5)$$

Where $I_o(hkl)$ represent the intensity of the standard peaks, $I(hkl)$ is the intensity of the bragg's

diffracted peaks for the synthesized samples and T.C. denotes the texture coefficient. The calculated values of T.C. are as shown Table 2.

Figure 2(b) shows the variation of texture coefficient with respect to miller indices. The value of texture coefficient greater than one specified the preferred orientation of the plane. Table 2 shows that the (111) plane is the preferred oriented plane.

3.2 Morphological analysis

The information related to the surface morphology of synthesized nanostructures is as given by scanning electron microscopy (SEM). As a result of high energy incident electron beam, a secondary beam of electrons as well as backscattered electrons are ejecting from the sample surface. The beam of secondary electrons provides information about the morphology of the synthesized samples. Sodium sulphide precursor based sample A shows the inhomogeneous distribution of nanoparticles²¹ whereas the thiourea based sample B shows flakes like morphology²² (Fig. 3). The cause of change in the morphology is due to the different growth rate pertaining to different preferred orientation of the miller planes which depends upon the choice of precursor. The morphology also affects the rate of inhibition towards the bacterial species. Sample B is more prominent to control the growth of bacterial species compared to sample A. The elemental analysis is done by energy dispersive X-ray spectroscopy as shown in Fig. 4. The average atomic and weight percent of the corresponding peaks for zinc and sulphur is given in Table 3. Absence of impurity peaks in the EDX spectra confirms the successful formation of the nanostructures.

3.3 UV-visible absorption spectroscopy

Optical studies are done to calculate the bandgap of the material and to study the presence of defect states. The UV-visible absorption spectroscopy uses a beam

Table 2 — Analysis of Texture Coefficient (T.C.)

hkl	T.C. (A)	T.C. (B)
(111)	1.12	1.31
(220)	0.79	0.88
(311)	1.08	0.78

Table1 — Average crystallite size, strain and dislocation density of the ZnS nanostructures.

Sample	angle(degrees)	FWHM β	Miller indices	Avg. crystallite size D(nm)	Strain ($\varepsilon \cdot 10^{-3}$)	Dislocation density ($\delta \cdot 10^{11}$)
A	28.62	2.38	(111)	3.88	0.0275	0.0667
	47.92	2.31	(220)			
	56.67	2.35	(311)			
B	28.83	2.91	(111)	3.05	0.0343	0.108
	48.29	2.75	(220)			
	57.16	3.33	(311)			

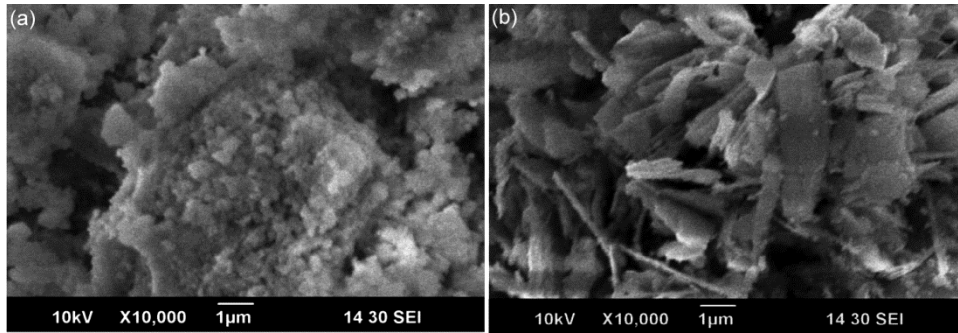


Fig. 3 — Morphology of ZnS nanostructures (a) sample A, and (b) sample B.

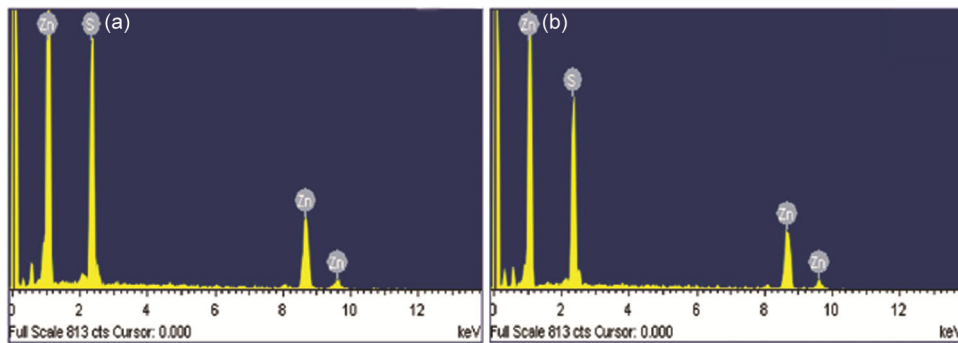


Fig. 4 — Elemental analysis of (a) sample A, and (b) sample B.

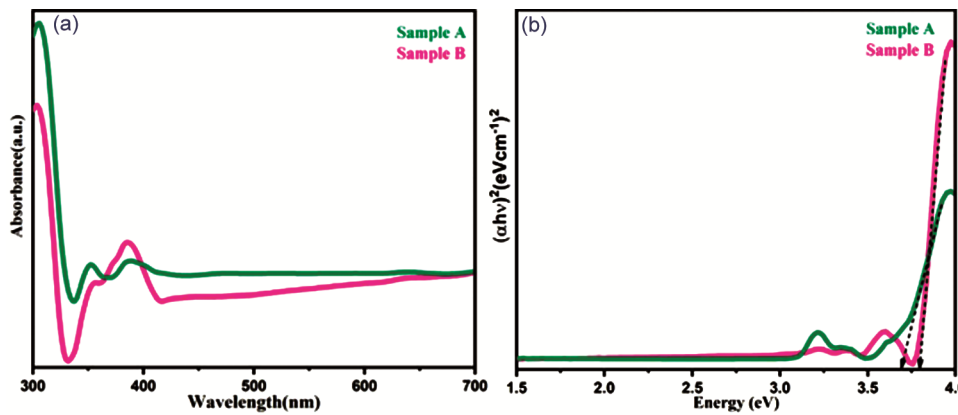


Fig. 5 — (a) UV-visible spectra, and (b) $(\alpha hv)^2 (eVcm^{-1})^2$ versus energy (eV) graph for bandgap calculation.

Table 3 — Atomic and weight percent of synthesized ZnS nanostructures.

Element	Sample A		Sample B	
	Weight%	Atomic%	Weight%	Atomic%
S K	34.58	51.86	31.42	48.29
Zn K	65.42	48.14	68.58	51.71
Totals	100.00		100.00	

of photon which is absorbed by the sample and the absorption spectra is obtained in the wavelength range 300 nm to 700 nm as shown in figure 5(a). For sample A, the absorption band is observed at 327 nm

and it is observed at 336 nm for sample B. To calculate bandgap Tauc and Menth²³ is used as given in equation 6

$$\alpha hv = k(hv - E_g)^{1/2} \dots (6)$$

The bandgap values are 3.79 eV for sample A and 3.68 eV for sample B measured by the tangent drawn to the energy axis as shown in the Fig. 5(b). Due to the high bandgap the generated electrons and holes in the conduction and valence band are unable to recombine and interact with the water molecules

present on the surface of the nanoparticles causes unwanted oxidation leads to the destruction of cell membrane of the bacteria.

3.4 Photoluminescence analysis

The photoluminescence spectrum is obtained in the wavelength range of 400nm to 650 nm as shown in Fig. 6. Both the samples are excited with the excitation wavelength of 320 nm. The sodium sulphide precursor based sample A show emission peak at 544 nm whereas the thiourea based sample B shows emission peak at 485 nm. The emission peak of thiourea based sample is more intense than that of sodium sulphide based sample and shifted to lower wavelength region²⁴⁻²⁵. The variation in luminescence intensity is due to the presence of defect centres in the forbidden gap of the material. The excitons got trapped in the defect centres leading to non radiative transitions and hence decrease in the luminescence intensity whereas; the increase in intensity is due to the radiative transitions. The emission peak observed at 470 nm for both the samples may be due to the presence of defects.

3.5 FTIR analysis

The presence of different functional groups attached to the sample is detected by fourier transform infrared spectroscopy which uses an infrared beam to detect the samples. The broad band presence at 3012 cm^{-1} and 3032 cm^{-1} is due to moisture present in the sample specified the O–H stretching mode of H_2O molecule. The bands due to asymmetrical and symmetrical stretching of zinc carboxylate COO^- are present at 1507 cm^{-1} , 1389 cm^{-1} and 1573 cm^{-1} , 1397 cm^{-1} for sample A and B respectively as shown in Fig. 7 the presence of bands at 645 cm^{-1} and 633 cm^{-1} is due to the Zn–S stretching vibration for

sample A and B respectively²⁶. Hence, the fourier analysis confirmed that the ZnS nanoparticles are successfully assembled to each other.

3.6 Antibacterial study

To scrutinize the antibacterial activity of ZnS nanostructures the well-diffusion method is used under indoor light- activation. Peptone, agar and yeast extract are added in distilled water and autoclaved to prepare nutrient agar solution which is further left to solidify on the petri dishes for overnight. The bacterial suspension is spread on the solidified agar plates using a sterilized swab and then a borer is used to insert wells on the solidified plates. The dissolved suspension of the samples is lodged into the wells using a micropipette and then placed in an incubator for 32 hours. The grey circular region is the zone of inhibition as shown in Fig. 8 which is larger in diameter for sample B than that of sample A as given in Table 4. Due to larger inhibition zone of sample B it is confirmed that the thiourea mediated sample is more effective to kill the bacterial species. The phenomenon responsible for cell death is the origination of reactive oxygen species (ROS). As the particle size of synthesized nanoparticles reaches to nano, the bandgap increases leads to the low recombination rate of prompted electron and hole pairs in conduction and valence band. The produced pairs hence come in contact with the water (H_2O) molecule present on the surface of the samples leads to the generation of hydroxide radicals (OH^\cdot) which penetrate the membrane of the cell causes cell death²⁷⁻²⁸. Hence, the synthesized samples successfully kill the bacterial families *E.coli* and *S.aureus* and may be further used for other

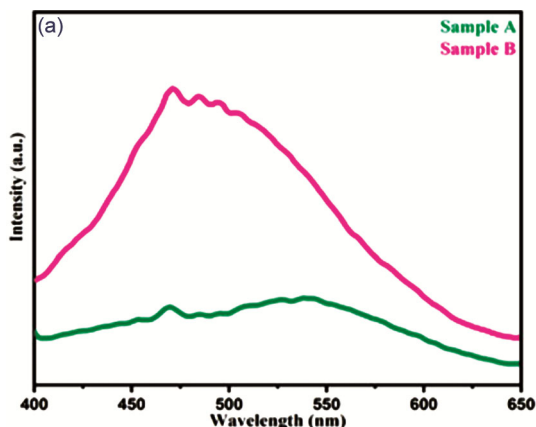


Fig. 6 — Photoluminescence spectroscopy.

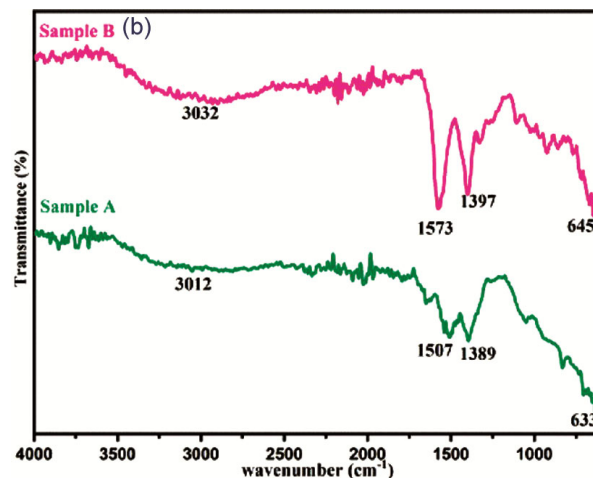


Fig. 7 — FTIR analysis of sample A and B.



Fig. 8 — The circular grey region is the zone of inhibition (ZOI) for Sample A and B with increased concentration against *E.coli* and *S. aureus*.

Table 4 — Zone of inhibition for sample A and B.

Sample	Inhibition zone	
	<i>S. aureus</i>	<i>E. coli</i>
A	15mm	16mm
B	16mm	18mm

applications such as an antioxidant and photocatalytic degradation etc.

4 Conclusion

Solvothermal method is used to synthesize zinc sulphide semiconducting nanostructures. The zinc blende crystal structure for both the samples is detected in the range of 20° to 70°. The agglomeration of nanoparticles with different morphology is observed by SEM. The atomic and weight percent of different elements present in the samples is given by EDX analysis. UV-visible absorption spectroscopy confirmed the bandgap value as 3.79 eV and 3.68 eV for the respective samples. The photoluminescence spectroscopy gives the emission peak in the visible region and the synthesized ZnS nanostructures are well assembled as detected by Fourier transform infrared spectroscopy. The synthesized nanostructures are efficient to kill the bacterial families *Escherichia coli* (*E. coli.*) and *Staphylococcus aureus* (*S. aureus*) and may be further used for other applications such as an antibiotic and an antioxidant etc.

Acknowledgement

The author, Lalita Rani is thankful to the department of microbiology, Kurukshetra university, Kurukshetra for providing the lab facilities to perform the antibacterial activity testing and an admirable thanks to Mr. Vinod (lab technician), NIT Kurukshetra for executing SEM and XRD machines.

The author is also thankful to UGC, New Delhi, India for providing fund in terms of senior research fellowship during my research work.

References

- Palani S, Rajamanickam A K & Kannappan G, *Int J Nano Dimens*, 13(4) (2022) 403.
- Mannodi- Kanakkithodi A *Model Simul Mat Sci Eng MODEL SIMUL MATER SC*, 30.4 (2022) 044001.
- Isshiki M, Wang J, *Springer handbook of electronic and photonic materials* Springer, Cham, (2017) 1.
- Afzaal M, O'Brien P, *J Mater Chem*, 16(17) (2006) 1597.
- Ruda H E, editor, *Springer Science & Business Media*, (Vol. 1) 1992.
- Rani L, Chauhan R P, *Surf Interfaces*, 33 (2022) 102306.
- Shah U, Jan F A, Ullah R, Ullah N, *J Solid State Sci Technol*, 11.3 (2022) 033011.
- Badawi A, Alharthi S S, *Superlattices Microstruct*, 151 (2021) 106838.
- Kumar S, Taneja S, Banyal S, Singhal M, Kumar V, Sahare S & Choubey R K, *J Electron Mater*, 50.7 (2021) 3986.
- Shakil M A, Das S, Rahman M A, Akther U S, Majumdar M K H & Rahman M K, *Mater sci appl*, 9.9 (2018) 751.
- Joseph A, Billakanti S, Pandit M A, Khatun S, Rengan A K & Muralidharan K, *Environ Sci Pollut Res*, (2022)1.
- Nehra P & Chauhan R P, *Magnetic Nanostructures*, (2019) 301.
- Vijayan S, Dash C S, Umadevi G, Sundararajan M & Mariappan R, *J Clust Sci*, 32.6 (2021) 1601.
- Kokilavani S, Al-Farraj S A, Thomas A M, El-Serehy H A, Raju L L & Khan S S, *Ceram Int*, 47.9 (2021) 12997.
- Wang C, Hu B, Chen L, Liu N & Li J, *Optik*, 224 (2020) 165673.
- Cullity B D, *Elements of X-ray Diffraction* (Addison-Wesley Publishing, 1956).
- Cullity B D, Addison-Wesley Publishing, 1956.
- Stokes A R, Wilson A J C, *Proc Phys Soc*, 56 (1944) 174.
- Williamson G K, Smallman R E, *Philos Mag 1* (1956) 34.
- Harris G B, *Philos Mag J Sci*, 43 (1952) 113.

- 21 Ganguly S, Das S & Dastidar S G, *Int J Pharm Therap*, 5 (2014) 230.
- 22 Kumari P, Sharma A, Kumawat A, Samanta S, Misra K P, Rao A & Chattopadhyay S, *Materials Today: Proceedings*, 58 (2022) 642.
- 23 Tauc J, Mentha A, *J Non Cryst Solids*, 8 (1972) 569.
- 24 Murugadoss G, *Particuology*, 11(5) (2013) 66.
- 25 Ramasamy V, Praba K & Murugadoss G, *Spectrochim Acta A Mol Biomol*, 96 (2012) 963.
- 26 Rani L & Chauhan R P, *J Clust Sci*, (2022)1.
- 27 Panthi G, Ranjit R, Khadka S, Gyawali K R, Kim H Y & Park M, *Adv Compos Hybrid Mater*, 3(1) (2020) 8.
- 28 Kumar G A, Naik H B, Viswanath R, Gowda I S & Santhosh K N, *Mater Sci Semicond Process*, 58 (2017) 22.